



Cardiac and respiration-induced brain deformations in humans quantified with high-field MRI

Jacob Jan Sloots^{a,*}, Geert Jan Biessels^b, Jaco J.M. Zwanenburg^a

^a Radiology, University Medical Center Utrecht, the Netherlands

^b Neurology, University Medical Center Utrecht, the Netherlands

ARTICLE INFO

Keywords:

Brain
Deformation
Tissue strain
Single-shot DENSE
Waste clearance
Microvasculature
Magnetic resonance imaging
Small vessel disease

ABSTRACT

Microvascular blood volume pulsations due to the cardiac and respiratory cycles induce brain tissue deformation and, as such, are considered to drive the brain's waste clearance system. We have developed a high-field magnetic resonance imaging (MRI) technique to quantify both cardiac and respiration-induced tissue deformations, which could not be assessed noninvasively before. The technique acquires motion encoded snapshot images in which various forms of motion and confounders are entangled. First, we optimized the motion sensitivity for application in the human brain. Next, we isolated the heartbeat and respiration-related deformations, by introducing a linear model that fits the snapshot series to the recorded physiological information. As a result, we obtained maps of the physiological tissue deformation with 3mm isotropic spatial resolution. Heartbeat and respiration-induced volumetric strain were significantly different from zero in the basal ganglia (median (25–75% interquartile range): $0.85 \cdot 10^{-3}$ ($0.39 \cdot 10^{-3}$ – $1.05 \cdot 10^{-3}$), $p = 0.0008$ and $-0.28 \cdot 10^{-3}$ ($-0.41 \cdot 10^{-3}$ – $0.06 \cdot 10^{-3}$), $p = 0.047$, respectively. Smaller volumetric strains were observed in the white matter of the centrum semi ovale ($0.28 \cdot 10^{-3}$ (0 – $0.59 \cdot 10^{-3}$) and $-0.06 \cdot 10^{-3}$ ($-0.17 \cdot 10^{-3}$ – $0.20 \cdot 10^{-3}$)), which was only significant for the heartbeat ($p = 0.02$ and $p = 0.7$, respectively). Furthermore, heartbeat-induced volumetric strain was about three times larger than respiration-induced volumetric strain. This technique opens a window on the driving forces of the human brain clearance system.

1. Introduction

Cardiac and respiratory cycles induce blood volume changes resulting in subtle brain tissue deformations. These deformations are known to propel the cerebral spinal fluid (CSF) flow which fulfills an important role in the drainage of cerebral waste (Mestre et al., 2017; Spector et al., 2015). Therefore, brain tissue deformation is considered an important driver of the clearance system of the brain (Tarasoff-Conway et al., 2015). Furthermore, brain tissue deformation affects cellular function. *In-vitro* studies have shown that the arterial waveform is crucial to regulate the formation and function of endothelial cells which constitute the blood-brain barrier (Dai et al., 2004). Brain tissue and vessel stiffness naturally change with age (Sack et al., 2011; Tsao et al., 2013), which not only plays a role in age-related processes but may also have profound effects on tissue deformation of the brain and, thus, brain homeostasis. Unlike the larger arteries of the brain, the small cerebral vessels themselves are difficult to study *in vivo* with current neuroimaging techniques. This is an important knowledge gap. We hypothesize that the brain tissue

deformation is dominated by the microvascular bed embedded in the tissue, and, thus provides a window to the small vessel function. We have developed a method to quantify brain tissue deformation that may form a valuable source of information on small vessel function as driving force in waste clearance, and may also allow for future assessment of the brain's biomechanics during both healthy and diseased state (Goriely et al., 2015).

The dynamic relationship between intracranial blood volume changes, tissue deformation and CSF flow is complex (Linninger et al., 2016). As the brain's vessels are exposed to blood pressure waves, they swell and stretch elastically, displacing the surrounding tissue. Due to the rise of the intravascular blood volume during systole, the cerebral tissue expands inwards towards the ventricles (Greitz et al., 1992; Feinberg and Mark, 1987; Ståhlberg et al., 1989). Given the fixed intracranial volume as stated by the Monro-Kellie doctrine, the CSF is squeezed out of the brain into the CSF spaces towards the spinal canal to compensate for the additional blood volume (Linninger et al., 2016; Mokri, 2001). As the blood leaves the brain during diastole, the vessels relax and CSF returns.

* Corresponding author. University Medical Center Utrecht Internal, E 01.132 P.O. Box: 85500 3508 GA, Utrecht, the Netherlands.

E-mail address: j.j.sloots-2@umcutrecht.nl (J.J. Sloots).

<https://doi.org/10.1016/j.neuroimage.2020.116581>

Received 12 August 2019; Received in revised form 23 December 2019; Accepted 20 January 2020

Available online 23 January 2020

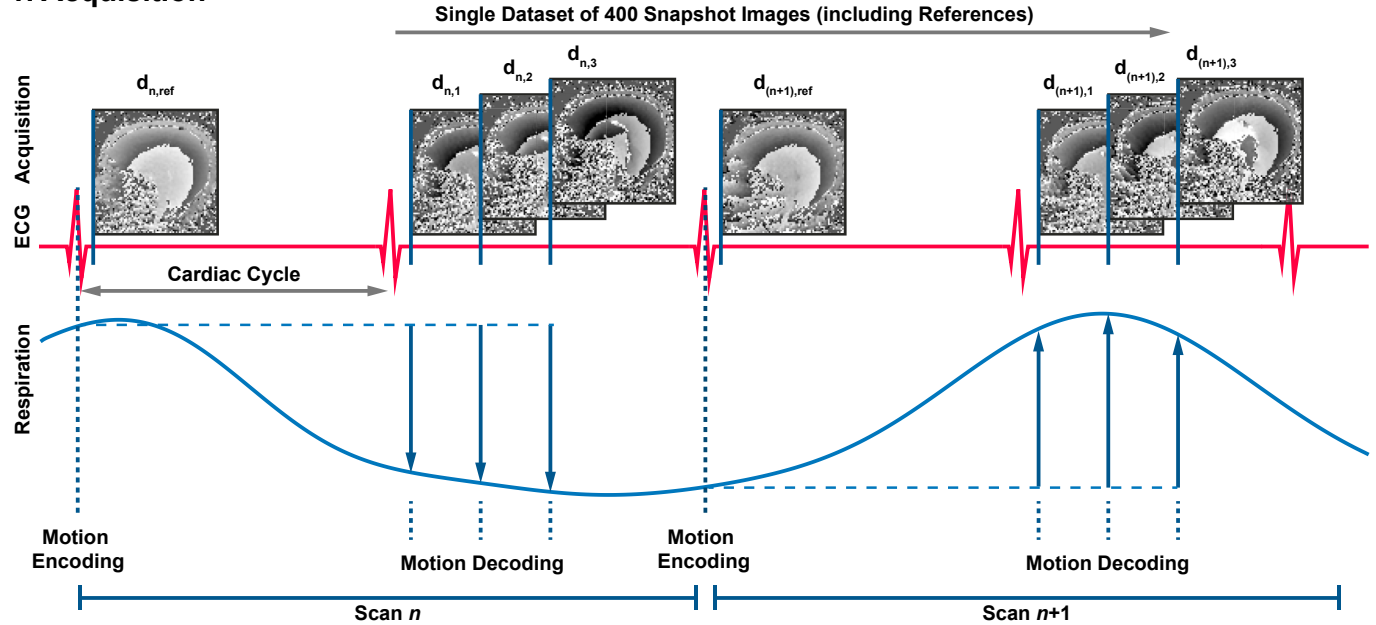
1053-8119/© 2020 The Authors. Published by Elsevier Inc. This is an open access article under the CC BY-NC-ND license (<http://creativecommons.org/licenses/by-nc-nd/4.0/>).

Similarly, the respiration cycles induce variations in thoracic pressure that cause variations in venous blood volume, which induces tissue deformation and CSF flow as well.

Despite the important role of the cardiac and respiration-induced brain tissue deformation in the intracranial dynamics, no methods are available to directly assess these deformations. Instead, most studies have

focused on CSF and blood flow to assess the intracranial volume dynamics (Alperin et al., 2000; Daouk et al., 2017). For instance, Dreha-Kulaczewski et al. used Magnetic Resonance Imaging (MRI) with phase contrast velocity encoding to study CSF flow and found upward CSF flow through the spinal canal during inspiration (Dreha-Kulaczewski et al., 2015, 2017), which they relate to an enhanced venous outflow.

1. Acquisition



2. Analysis

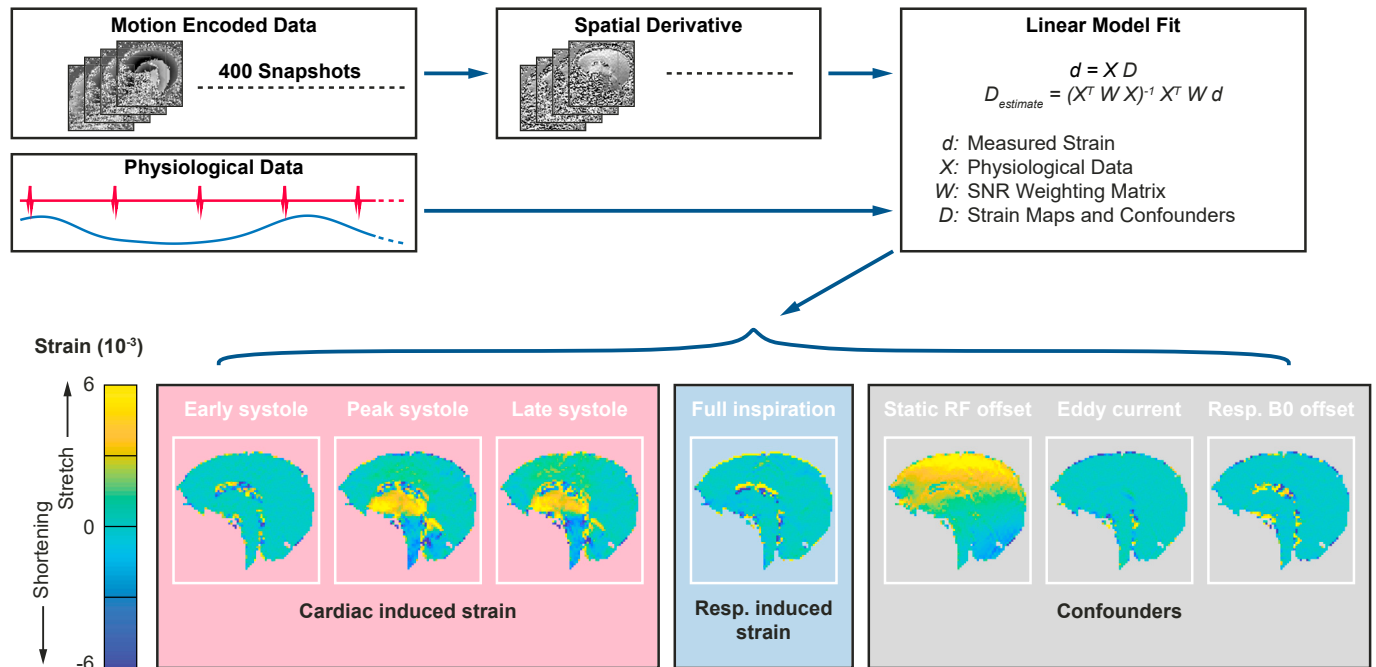


Fig. 1. Example for data acquisition and analysis of one of the volunteers. The DENSE MRI sequence was used to encode motion into the phase of the MRI signal.

- (1) Data was recorded over 100 dynamics (one slice, Feet-to-Head motion encoding direction) with alternating encoding direction sign to distinguish between phase contributions due to motion and motion independent phase confounders. Per dynamic scan, three snapshot DENSE images were acquired at different moments in the cardiac cycle together with the associated physiological data (see example traces). Also, a reference image was acquired directly after encoding to allow for corrections of potential eddy current effects.
- (2) Time-series of displacement-encoded phase images were used to derive the strain maps by computing the spatial derivative along the encoding direction. Together with the associated physiological data, these strain maps were used in a linear model to isolate the components of cardiac and respiration-induced strain. Including the confounders, the linear model produced seven maps.

Furthermore, T_2^* -weighted blood oxygen level dependent (BOLD) MRI signal fluctuations in the brain have been studied in relation with physiological signals like heartbeat and respiration (Polimeni et al., 2016; Kiviniemi et al., 2016; Bianciardi et al., 2009). These T_2^* -weighted signals, however, are not specific and depend on blood oxygenation levels (spontaneous neuronal activity), inflow of blood and CSF into the slice, and tissue motion. As a result, T_2^* -weighted signal variations in the brain are hard to interpret, and only weakly correlate with physiological cycles like heartbeat and respiration (Bianciardi et al., 2009). Quantitative measurements of T_2^* variation induced by the cardiac cycle have also been reported, either with or without injection of a blood pool contrast agent (Rivera-Rivera et al., 2019; Viessmann et al., 2017). These quantitative T_2^* measurements are much more specific for blood volume pulsations compared to BOLD MRI, but still did not assess the changes due to respiration. The overall deformation of brain tissue is subtle and involves submillimeter displacements that can be tracked by an MRI technique that is called Displacement Encoding with Stimulated Echoes (DENSE) (Reese et al., 2002; Fischer et al., 1993; Aletas et al., 1999). The cardiac-gated DENSE method was shown to be capable of capturing the displacement field maps over the cardiac cycle (Soellinger et al., 2009; Pahlavian et al., 2018; Adams et al., 2019). However, these data were acquired over several minutes, which prohibits to study the respiration-induced tissue motion and deformation.

In the present study, we propose a newly developed DENSE sequence at 7T MRI, dedicated and optimized to disentangle and quantify cardiac and respiratory contributions to brain tissue deformation in humans (Fig. 1). A key feature is its single-shot approach, which not only is required for unraveling the cardiac and respiratory contributions, but also allows for an optimization of the sequence without introducing additional data artifacts. The main advantage of our sequence is the separate assessment of both cardiac and respiratory tissue strain contributions with high sensitivity, which provides insight into the physiological brain tissue deformations in relatively small regions of interest (ROIs).

2. Materials and methods

Displacement images are required to derive the tissue deformation and can be provided by the DENSE MRI sequence (Fischer et al., 1993; Aletas et al., 1999; Soellinger et al., 2009; Adams et al., 2019; Sloots et al., 2019a). DENSE, analogous to phase contrast velocity encoding, manipulates the phase information such that it becomes proportional to the displacement of brain tissue with respect to the point of encoding. The single-shot approach of our sequence captures the momentary physiological ‘state’ of tissue motion. We assume that this physiological ‘state’ of the tissue is an independent, linear combination of the cardiac and respiratory contributions. By repeating the measurements multiple times, we acquired different combinations of states. Next, we use a linear model, together with the associated physiological information, such as cardiac interval position and respiration trace, to disentangle the cardiac and respiratory contributions (Fig. 1).

2.1. DENSE sequence

A cardiac triggered DENSE sequence was designed to measure heartbeat and respiration-related brain tissue motion (Fig. 2) (Fischer et al., 1993; Aletas et al., 1999; Soellinger et al., 2009; Adams et al., 2019; Sloots et al., 2019a). Key features included its 2D single-shot EPI approach to capture the momentary physiological ‘state’ (cardiac and respiration-induced motion) and secondly, an additional time-delay of one cardiac cycle between encoding and decoding to make the sequence more sensitive for respiration-induced motion contributions.

The DENSE sequence (Aletas et al., 1999) consists of a motion encoding and -decoding part. The encoding part encodes the tissue’s current position in the longitudinal magnetization by using two RF pulses with an encoding gradient (G_{enc}) in between. After a given mixing time, the decoding part reads out the prepared longitudinal magnetization by using another RF pulse followed by a decoding gradient (G_{dec}) that is equal to G_{enc} . Any tissue displacement along the direction of these

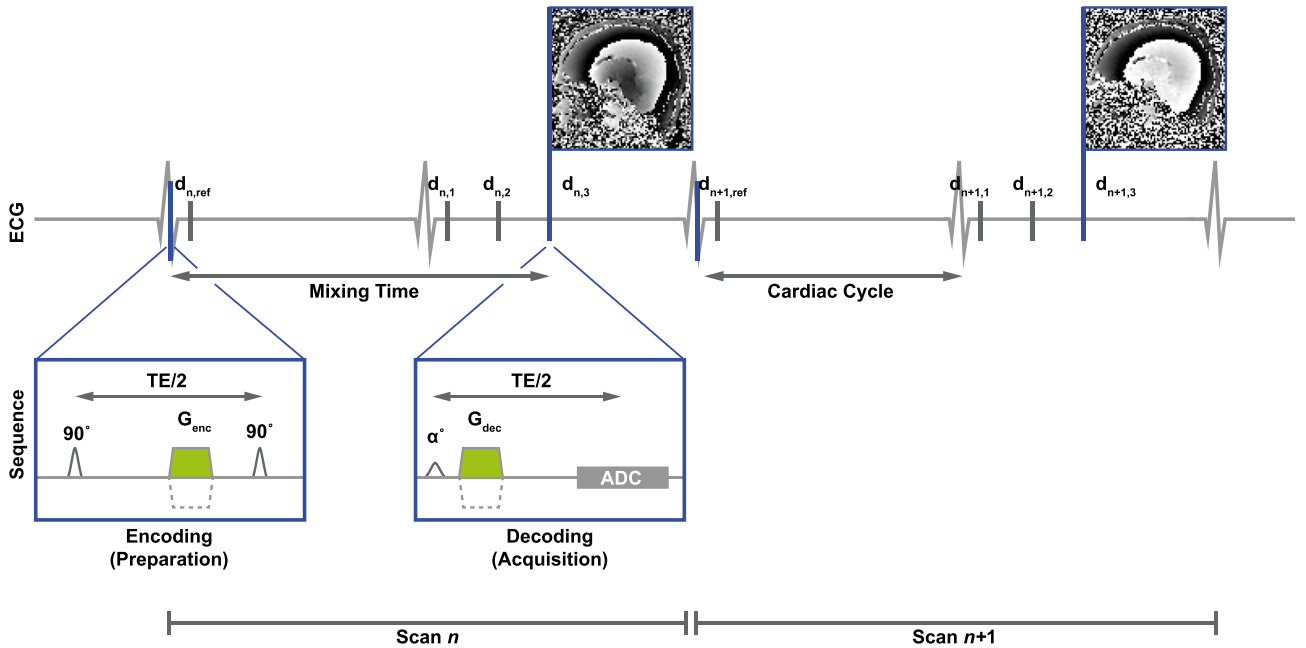


Fig. 2. Schematic representation of the developed 2D single-shot DENSE sequence, covering two dynamic scans (n and $n+1$) that each comprise two cardiac cycles. The tissue’s initial position is encoded in the longitudinal magnetization at the beginning of the dynamic scan, by the encoding gradient G_{enc} in the preparation part of the sequence. The prepared magnetization is decoded in the next cardiac cycle by the acquisition part of the sequence, which uses another RF pulse for signal excitation, followed by a decoding gradient (G_{dec}) that is equal to G_{enc} . Any tissue displacement along the direction of these gradients that occurs between G_{enc} and G_{dec} (during the so-called ‘mixing time’) leads to a corresponding phase shift in the resulting phase image. The DENSE images are acquired during the next cardiac cycle to increase the sensitivity to respiratory motion together with a reference phase directly after encoding to allow for potential eddy current corrections. Both encoding and decoding gradients G were inverted every two dynamics (dashed lines), to distinguish phase contributions due to motion from phase contributions due to confounding factors.

gradients that occurred between G_{enc} and G_{dec} leads to a corresponding phase shift in the resulting phase image. The encoding- and decoding gradient alternated in sign every other dynamic to distinguish between phase contributions due to motion and confounding phase contributions from other sources (static RF phase, phase induced by off-resonance effects, and dynamic phase variation induced by respiration-related B_0 fluctuations (Van Gelderen et al., 2007)). The signal from fat tissue was avoided through the use of low bandwidth (500 Hz) RF pulses during encoding, yielding water-selective tagging. Thus, we avoided artifacts from high fat signal close to the receiver elements of the head coil.

2.2. Data acquisition

The Ethical Review Board (ERB) of the University Medical Center Utrecht approved the use of healthy volunteers for MRI protocol development. Nine healthy volunteers (6 males, 3 females, age 29 ± 3 years) were included and written informed consent was obtained in accordance with the ERB approval. The volunteers were scanned at 7T (Philips Healthcare, Best, The Netherlands) using a 32-channel head coil (Nova Medical). A single DENSE dataset consisted of 100 dynamic scans with 4 motion decoded snapshots per dynamic, resulting in 400 snapshots over time, and a scan-duration of 2.5–5 min, depending on the heart rate (80–40bpm). Other acquisition parameters were: EPI factor: 33; SENSE factor: 2.5 (AP or RL); resolution: $3 \times 3 \times 3 \text{ mm}^3$; FOV: $250 \times 250 \text{ mm}^2$; TE/2: 12 ms and BW: 61.9 Hz/pixel. A sagittal and perpendicular coronal slice were planned, and displacement images were separately acquired with two in-plane encoding directions. As a result, four 1D motion-encoded datasets were recorded: two datasets from a sagittal slice with 1D motion encodings in the Feet-to-Head and Anterior-to-Posterior direction respectively, and two datasets from a coronal slice with 1D motion encodings in the Feet-to-Head and Right-to-Left direction, respectively. The sagittal slice was planned 10mm from the interhemispheric fissure of the brain and aligned with the brain stem (Fig. 3 for planning details). The volunteers were asked for a calm abdominal breath during the experiment. Physiological data was simultaneously recorded by using a vector cardiogram (VCG) for triggering and a respiration belt to trace abdominal breathing. Additionally, a pulse oximeter was placed on the left index or middle finger as additional input in the analysis to cope with missed VCG triggers.

After encoding of the signal, three frames were acquired in the next cardiac cycle at respectively 0, 25 and 50% of the average cardiac interval. To allow for corrections of potential eddy current effects, an additional reference frame was acquired directly after encoding. Although the signal intensities of the successive frames are affected differently by T_1 -relaxation and diffusion-related signal attenuation, this does not affect the displacement information. Yet, the SNR present in the displacement images ($\text{SNR}_{\text{displ}}$) relates to the SNR in the magnitude images (SNR_M). To obtain a stable SNR over the acquired frames, a variable excitation flip angle scheme was recursively calculated (Sloots et al., 2019b), starting from the final flip angle α_{max} . Furthermore, the tag spacing T_{enc} (in units mm/π) summarizes the sensitivity for the spatial displacement encoding. Large encoding gradients yield an increased displacement sensitivity (smaller T_{enc}), yet, they reduce the SNR of the magnitude image due to their large b-values (diffusion sensitivity) (Bammer, 2003).

2.3. Sequence optimization for strain estimates

The tissue deformation is physically described as strain, which signifies local stretch (positive strain) and shortening (negative strain) of tissue. The one-dimensional (1D) strain ϵ is simply the change in length of a line segment L and defined to give the relative change in length of the line segment during deformation

$$\epsilon = \frac{L' - L}{L} = \frac{\Delta L}{L} \quad (1)$$

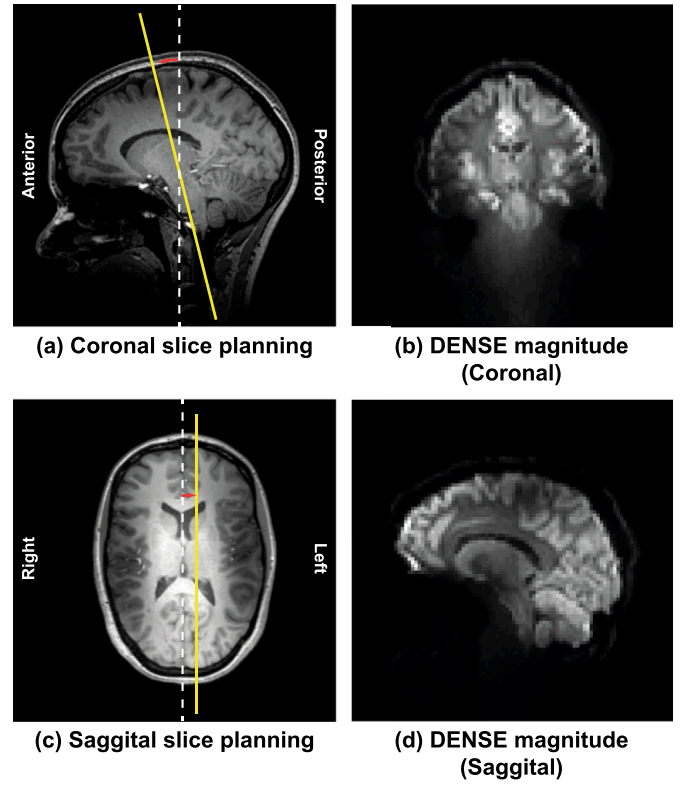


Fig. 3. Slice planning of the 2D DENSE scans with respect to the whole-brain 3D T_1 -weighted TFE planning scan. The yellow lines indicate the planned slices with respect to the interhemispheric fissure, which is indicated by the white dotted line. **a)** The coronal slice was planned through the brain stem as indicated in the figure (parallel to the brain stem; subject dependent RL angulation of 12–14°). **c)** The sagittal slice was planned perpendicular to the coronal slice, 10mm from the interhemispheric fissure towards the left. **b,d)** The DENSE magnitude image as acquired, averaged over all acquisitions.

where L is the original length of the line segment and L' is the length of the line segment after deformation. The strain is obtained from displacement images by calculating spatial derivatives. Given Δx , the voxel size along x , we can define the 1D strain in that direction as

$$\epsilon_{xx}(n) \stackrel{\text{def}}{=} \frac{D_x(n+1) - D_x(n-1)}{2\Delta x} \quad (2)$$

Accurate measurements are crucial, since the computation of spatial derivatives amplifies noise present in the displacement images. Larger encoding gradients yield an increased displacement sensitivity (smaller T_{enc}), yet, increase the number of phase wraps present in the displacement maps. Fortunately, strain computations allow for straightforward unwrapping under the assumption of small strains, as any phase wrap in the original image yields unlikely high strain values. A phase wrap causes a large numeric derivative $\Delta\phi$, which was resolved by adding or subtracting 2π to $\Delta\phi$ to bring it closer to zero if

$$|\Delta\phi| > 1.5\pi = \Delta\phi_{\text{max}} \quad (3)$$

The maximum tolerated numeric derivative $\Delta\phi$ relates to the maximum tolerated strain by

$$\epsilon_{\text{max}} = \frac{\Delta\phi_{\text{max}}}{2\Delta x} \frac{T_{\text{enc}}}{\pi} = 0.75 \frac{T_{\text{enc}}}{\Delta x} \quad (4)$$

Thus, as long as the expected strains in the brain do not exceed ϵ_{max} , there are no additional constraints for the encoding sensitivity. However, although larger encoding gradients yield an increased displacement

sensitivity, they reduce the SNR of the magnitude image due to their larger diffusion sensitivity (expressed by its b-values). Similarly, a larger final flip angle increases the excited signal, but prevents regrowth of magnetization for the next encoding. Consequently, an optimal T_{enc} and final flip angle exists for a given apparent diffusion coefficient (ADC) and longitudinal relaxation time constant (T_1) of the tissue.

We simulated the DENSE sequence for different settings of T_{enc} and α_{max} and found optimal DENSE sequence settings of $T_{enc} = 0.15\text{mm}/\pi$ and $\alpha_{max} = 50^\circ$ (white matter: $T_1 = 1200\text{ ms}$ and $\text{ADC} = 0.8 \cdot 10^{-3}\text{mm}^2/\text{s}$ at 7T (Rooney et al., 2007) (Helenius et al., 2002)) for acquiring strain images (Sloots et al., 2019b). The T_1 and ADC of white matter was chosen as this has a shorter T_1 than gray matter and, thus, faster decay of the tagged magnetization. We verified our simulations in a phantom (Sloots et al., 2019b) for which we used a multi-shot 3D EPI imaging protocol with imaging parameters: EPI factor: 19; SENSE factor: 2.6×2.5 (AP x RL); resolution: $3 \times 3 \times 3\text{mm}^3$, FOV $150 \times 150 \times 150\text{mm}^3$; and TE/2: 15 ms.

2.4. Linear model

The linear model will be described starting from the two example images outlined in Fig. 2. These two images represent the phase of the DENSE images acquired at 50% of the cardiac interval. Due to an alternating encoding direction, the second acquired image has an opposite phase contribution due to motion compared to the first image. This way, we can distinguish between phase contributions due to motion and static phase confounders. The phase image is converted to a displacement image by multiplying the phase image with T_{enc}/π . The cardiac-related displacement map can be separated from the confounding background by modelling each of the two example images as a linear combination of the cardiac-related displacement map ($D_{c,3}$) and the static displacement confounder (D_0):

$$d_{n,3} = x_0 D_0 + x_{c,3} D_{c,3} \quad (5)$$

The above equation represents the apparent total tissue displacement $d_{n,i}$ of snapshot i acquired in dynamic scan n (for the current example, $d_{n,3}$ represents the apparent motion in the only snapshot in dynamic n as shown in Fig. 2). D_0 is the apparent displacement due to static RF phase errors and $D_{c,3}$ is the cardiac-related displacement at the third time point in the cardiac cycle (which corresponds to 50% of the cardiac interval). The associated coefficients x are known, and required to estimate the displacement maps from the measured data. The coefficient x_0 is 1 for both images, whereas $x_{c,3}$ alternates in sign depending on the sign of the motion encoding gradient. The matrix formulation of the model for the two example images then yields

$$\begin{bmatrix} d_{n,3} \\ d_{n+1,3} \end{bmatrix} = \begin{bmatrix} 1 & 1 \\ 1 & -1 \end{bmatrix} \begin{bmatrix} D_0 \\ D_{c,3} \end{bmatrix} \quad (6)$$

The equation in this example is easily solved by simple inversion. However, we will acquire many more measurements than unknowns, which will result in the descriptive matrix not being square. Therefore, we solve this equation for D_0 and $D_{c,3}$ using the Least-Squares estimation method if more than two dynamic scans are performed. The method thereby provides the displacement at 50% of the cardiac cycle ($D_{c,3}$) together with the apparent displacement induced by static phase errors (D_0).

The model easily expands to incorporate the additional displacement images at 0 and 25% of the cardiac cycle. In addition to the displacement induced by the cardiac cycle, we incorporate the displacement induced by respiration. We assume that the respiration-related displacement depends linearly on the difference in respiration trace between encoding and decoding of the signal and is independent of the cardiac-related displacement. We base this assumption on preliminary results where we analyzed the residuals of a model without respiration adaptation and found that the residual tissue displacements showed a linear dependence on the difference in respiration trace (between encoding and decoding). The term D_{resp} represents this linear respiration contribution.

Furthermore, we include two additional correction terms. Firstly, an eddy-current offset term D_{eddy} to account for phase errors induced by the high decoding gradient and secondly, a respiration-induced B_0 offset term $D_{0,resp}$ (Van Gelderen et al., 2007). The complete model then yields

$$d_{n,i}(c, r) = D_0 + x_{eddy} D_{eddy} + \sum_{i=1}^3 x_{c,i} D_{c,i} + x_{resp} D_{resp} + x_{0,resp} D_{0,resp} \quad (7)$$

The physiological data and sequence design provide the values of the weighting factors x . The weighting factors x_{eddy} , $x_{c,i}$ and x_{resp} have alternating signs related to the alternating sign of the motion encoding gradients. If coefficient ξ represents this sign, then $x_{c,i} = \xi$ for $i = 1, 2$ or 3 , for a frame acquired at 0, 25 or 50% of the associated actual cardiac interval, respectively. Still, due to a varying heart rate during acquisition, frames can fall between these intervals. In that case, cardiac weighting factors are linearly interpolated such that

$$\begin{aligned} 0 &\leq |x_{c,i}| \leq 1 \\ \sum_{i=1}^3 |x_{c,i}| &= 1 \end{aligned} \quad (8)$$

The respiration weighting factors are described by $x_{resp} = \xi \Delta \varphi r$ (which accounts for respiration-induced motion, with alternating sign ξ) and $x_{0,resp} = \Delta r$ (which accounts for respiration induces resonance shifts (Van Gelderen et al., 2007)), where Δr is the normalized difference in abdominal respiration position between encoding and decoding. For clarity, we provide the matrix formulation for the extended linear model representing the 8 motion-encoded snapshot images in Fig. 1.1. This extended model is used to unravel cardiac and respiratory contributions to the displacement of brain tissue.

$$\begin{bmatrix} d_{n,ref} \\ d_{n,1} \\ d_{n,2} \\ d_{n,3} \\ d_{n+1,ref} \\ d_{n+1,1} \\ d_{n+1,2} \\ d_{n+1,3} \end{bmatrix} = \begin{bmatrix} 1 & 1 & 0 & 0 & 0 & 0 & 0 \\ 1 & 1 & 1 & 0 & 0 & -0.75 & -0.75 \\ 1 & 1 & 0.02 & 0.98 & 0 & -0.80 & -0.80 \\ 1 & 1 & 0 & 0.05 & 0.95 & -0.85 & -0.85 \\ 1 & -1 & 0 & 0 & 0 & 0 & 0 \\ 1 & -1 & -1 & 0 & 0 & -0.10 & 0.10 \\ 1 & -1 & 0 & -0.94 & -0.06 & -0.85 & 0.85 \\ 1 & -1 & 0 & 0 & -1 & -0.65 & 0.65 \end{bmatrix} \begin{bmatrix} D_0 \\ D_{eddy} \\ D_{c,1} \\ D_{c,2} \\ D_{c,3} \\ D_{resp} \\ D_{0,resp} \end{bmatrix} \quad (9)$$

2.5. Analysis

The acquired time series were analyzed offline with custom MATLAB R2018b software (The MathWorks, Inc., Natick, MA, USA). The VCG and POx trigger moments as recognized by the scanner software were used to deduce the positions of the snapshot images relative to the cardiac interval. VCG triggering sometimes failed due to magneto hemodynamic effects. The associated images were retrospectively discarded by using only the images for which the related VCG triggers were accompanied by a POx trigger occurring within 200 ms and 400 ms after the VCG trigger. The respiration change between encoding and decoding was deduced from the recorded respiration trace, which was filtered with a band-pass filter with cut-off frequencies at 0.1 and 1 Hz. Furthermore, the respiration was normalized by using the interval between the minimum and maximum observed value of the respiration trace, after discarding the lowest and highest 2.5% of its values. The remaining interval is referred to as the 95% range of the respiration trace, which served as normalization. Thus, the respiration-related coefficients in design matrix X had values ranging from just under -1 to just over 1 . The estimated map D_{resp} , thus, represents the induced motion for a – by definition – ‘full’ inspiration (change of respiration coefficient from 0 to 1). Similarly, the effect of expiration can be found by multiplying the estimated map D_{resp} by -1 (change of respiration coefficient from 0 to -1).

The dynamic scans of DENSE images were registered with a rigid in-plane whole-voxel transformation using elastix (Klein et al., 2010). All

sagittal slices were registered to the last sagittal dynamic scan, whereas all coronal slices were registered to the first coronal dynamic scan, which was acquired subsequently to the last sagittal dynamic scan. No corrections for geometric EPI-distortion were performed, as we analyzed only small ROIs in regions with very low B_0 inhomogeneity. Strain images were obtained by computing the spatial derivative from the displacement images along the encoding direction, where derivatives larger than $0.75 \cdot T_{enc} / \Delta x$ were unwrapped. From the unwrapped strain images, the various motion contributions and confounders were unraveled voxelwise by computing the pseudoinverse (least-squares) of X that contained the physiological information at each measurement.

$$D_{estimate} = (X^T W X)^{-1} X^T W d \quad (10)$$

Here, d is the measured data (either (apparent) displacement or strain images) and W represents the weighting matrix accounting for the variable SNR in the different snapshots in each voxel. The values in the weighting matrix W consisted of the normalized SNR (proportional to the magnitude signal squared) in each voxel associated with the measurement for the displacement data. For the strain data, these values corresponded to the mean SNR of the two voxels that were used to compute the derivative. This way, W corrects for SNR differences caused by, among others, the spatial variation in flip angle due to the dielectric effects present at 7T. The model was solved voxel-wise which resulted in seven maps: 4 maps of displacement or strain (depending on the input data) and 3 maps of confounders as illustrated in Fig. 1. An inter-subject comparison was then performed in two ROIs; one in the centrum semi ovale (CSO) and one in the basal ganglia (BG). To reduce the effect from noise in the strain maps, the median in each ROI was used for the analysis. Furthermore, the dependence of the strain in the Feet-to-Head direction on the ROI selection was tested by evaluating the FH strain along the entire intersection line of the sagittal and

coronal slice.

3. Results

3.1. The linear model: example for displacement maps

For illustrative purposes, the linear model was applied to the motion-encoded snapshot images, following the procedure of Fig. 1 without computing any derivatives. An important constraint for correctly fitting the displacement maps is that the motion-encoded snapshot images are correctly unwrapped. To this end, the images were acquired with lower encoding sensitivity ($T_{enc} = 0.25\text{mm}/\pi$) than optimal for strain (optimal for strain: $T_{enc} = 0.15\text{mm}/\pi$) to avoid phase wraps.

The linear fit resulted in four smooth displacement maps (cardiac and respiration-induced) and three confounding factors: a static RF phase offset, phase induced by off-resonance effects and a respiration-induced B_0 offset fluctuation ranging typically between 0 and 10 Hz from the base of the brain to the top of the brain (Fig. 4). In the displacement map associated with a full inspiration, we observed a translation of the complete head in the Feet direction together with a slight rotation, where the back of the head moves in the Head direction and the front of the head moves in the Feet direction. However, mere translations and rotations of the head are not considered to drive any brain clearance. Therefore, tissue deformation will be considered for the remainder of this study.

3.2. Validation of DENSE optimization

We found SNR_M to be consistent with computer simulations for both a variable final flip angle α_{max} and encoding sensitivity T_{enc} (Fig. 5a and b, respectively). The simulated SNR_{displ} for both the phantom and white matter is shown in Fig. 5c as a function of the tag spacing. All sequence-dependent SNR behavior not related to T_{enc} or α_{max} is represented in a

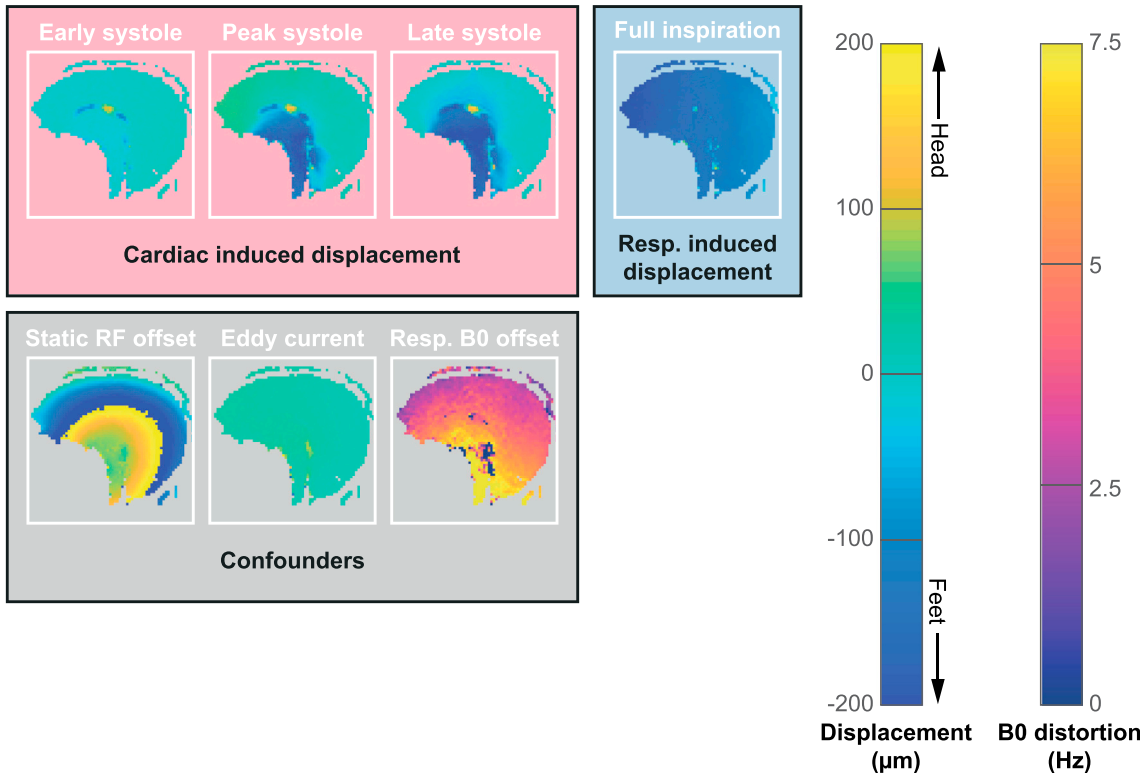


Fig. 4. Feet-to-Head motion maps of subject 1, produced with a dataset that had lower encoding sensitivity (tag spacing: $0.25\text{mm}/\pi$) than optimal for strain (optimal for strain: $0.15\text{mm}/\pi$) to avoid phase wraps. The images are from the same subject as in Fig. 1. For the current figure, the spatial derivative was not performed before fitting the linear model, in order to obtain motion maps rather than strain maps. The top row shows the cardiac and respiratory motion, respectively, whereas the bottom row represents the phase confounders. The dynamic B_0 offset fluctuations due to respiration are scaled in Hz, for comparison with literature (Van Gelderen et al., 2007).

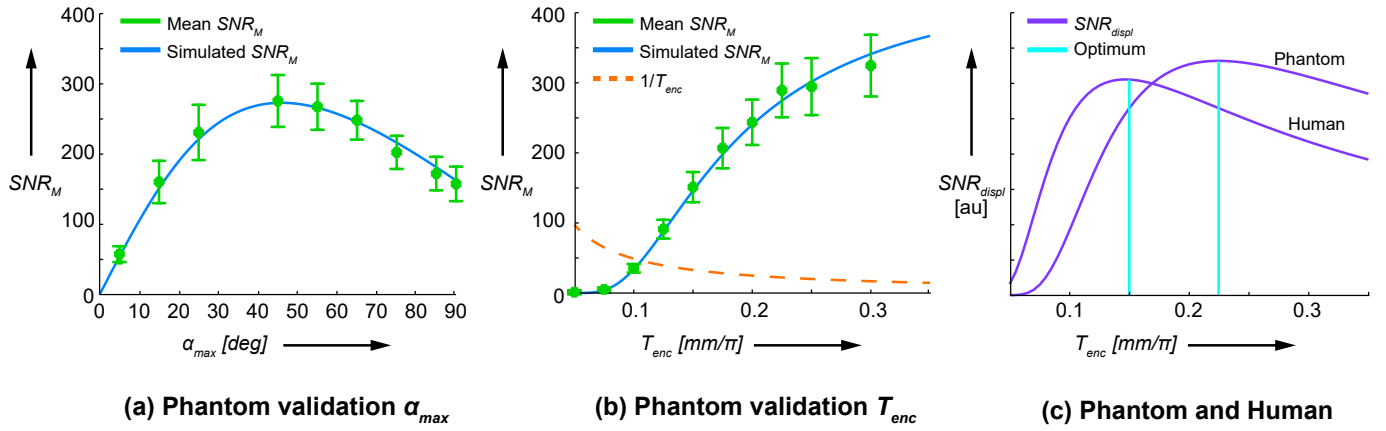


Fig. 5. Signal to noise ratio of the magnitude image (SNR_M) and displacement map (SNR_{displ}) with error bars indicating the standard deviation. a,b) Simulated SNR_M with the SNR_M observed in the phantom. The simulated SNR line was linearly scaled to match the measured SNR_M in the phantom. The results show that the course of the line matches the measured SNR behavior. c) Simulated SNR_M divided by the tag spacing, which matches the SNR in the displacement map. The optimum is shown for both the phantom and white matter in humans at 7T.

linear scaling parameter that matches the measured SNR_M with the SNR_M observed in the phantom.

3.3. Strain anisotropy

Cardiac-related strain was largest at peak systole (25% of the cardiac interval) and was compared with strain induced by a full inspiration (95% range of the respiration trace). Fig. 6 represents the resulting strain maps at peak systole for volunteer 1, two of which are in the sagittal plane and the other two in the coronal plane. The ROIs for inter-subject comparison are indicated as well. To capture the physiological 3D anisotropic tissue deformations, we combined the results in these ROIs along the intersection line from two orthogonal slices with different encodings.

Fig. 7a–b shows the strain in the three orthogonal directions

separately. The dependence of FH strain on the ROI selection was tested by evaluating the FH strain along the entire intersection line of the sagittal and coronal slice. The results showed a smooth curve and narrow interquartile ranges in regions where no CSF was present (see [Supplementary Fig. S1](#)). In the selected ROIs, the cardiac-induced tissue deformation at peak systole (Fig. 7a) shows anisotropic strain with expansion in the Feet-to-Head direction and minor compression in the other two directions. This observation is also known as the Poisson effect, where axial expansion of an object in the direction of the expansion load is accompanied by transverse compression. Although much smaller, we observed a similar but opposite trend for the respiration-induced strain (Fig. 7b). For a full inspiration, the tissue contracts in the Feet-to-Head direction and expands in the other two directions. By design of the model, a full expiration would invert this trend. The tissue strains induced by the cardiac cycle are much larger compared to the strains

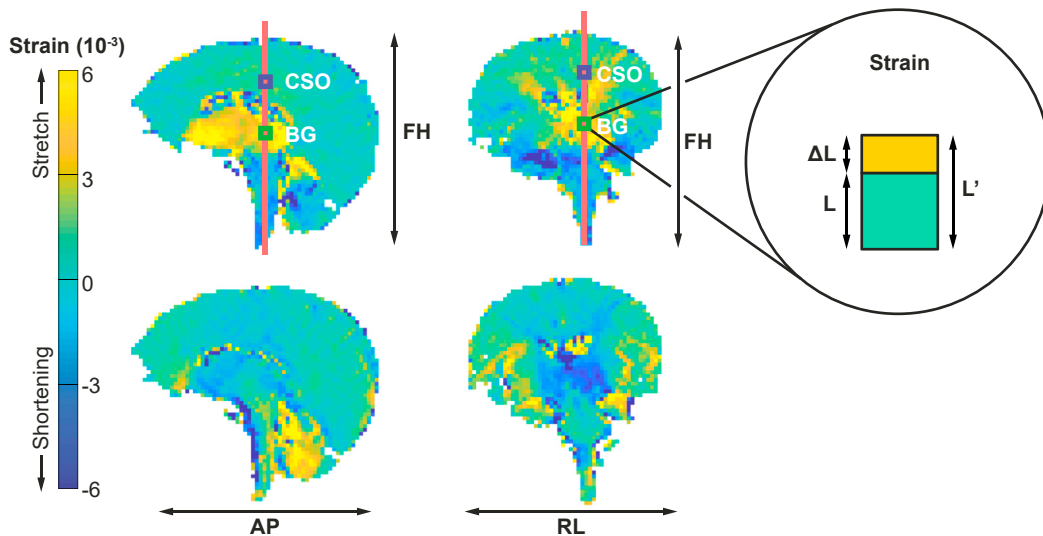


Fig. 6. Four fitted 1D strain maps of one volunteer in three motion encoding directions for sagittal (left column) and coronal (right column) slice at peak systole. Two ROIs, one in the centrum semi ovale (CSO) and one in the basal ganglia (BG) (top-row), were manually selected per subject and used for further strain analysis. Each map represents the 1D strain calculated as the spatial derivative along the associated motion encoding direction, which is indicated by the black arrows. The one-dimensional strain is illustrated in the circled area and represents the change in length, ΔL , of a line segment L . The strain ϵ is defined as the relative change in length of the line segment during deformation (see [Eq \(1\)](#)).

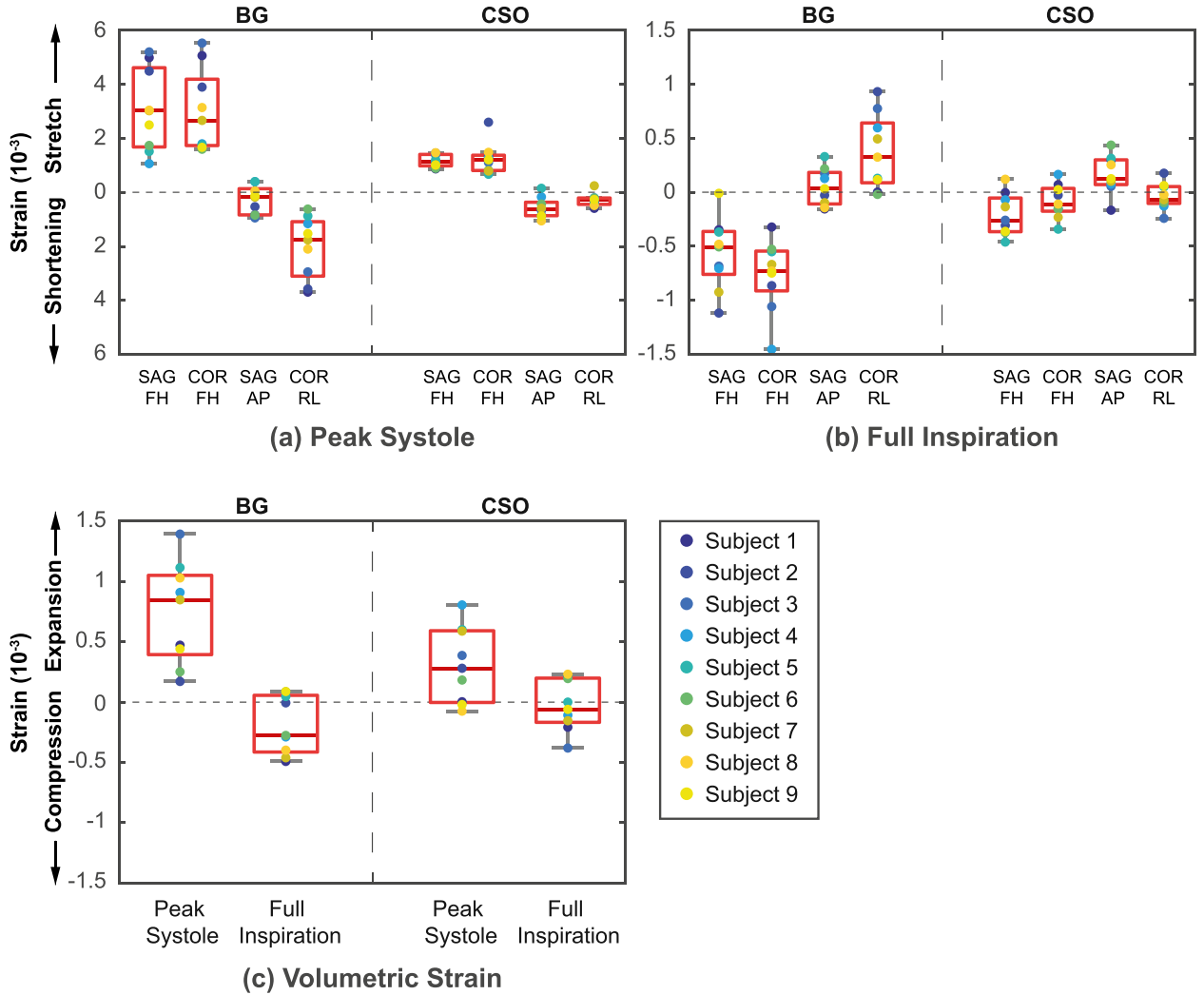


Fig. 7. Strain-measurement results at peak systole and for a full inspiration. The model was designed such that a full expiration would contribute the same as minus a full inspiration. (a–b) 1D strains (ROI medians) shown for the three perpendicular motion encoding directions in the BG and CSO. The FH direction was measured twice, once in the sagittal oriented slice (SAG), and once in the coronal oriented slice (COR). The similar results for both FH acquisitions indicate good reproducibility of the measurements. The different colors represent different subjects. Figure a and b show the cardiac and respiration contributions, respectively. Please note the difference in scale along the y-axis. For cardiac-induced strain, the Feet-to-Head direction shows relatively large expansion, whereas the other two directions show some compression (this is known as the Poisson effect). The effect is most pronounced in the BG, yet is of the same trend in the CSO. Interestingly, the respiration-induced strain shows a similar but opposite trend, consistent with outflow of (venous) blood with inspiration, due to lower thoracic pressure. (c) Volumetric strain analysis for nine subjects. The volumetric strain was obtained by summing over the 1D strains from all 3 encoding directions. For each 1D strain direction, the median over the associated ROI indicated in Fig. 6 was used. (For the Feet-to-Head direction, the median of the combined ROIs of both the coronal and sagittal slice was used). The left two boxes represent the results in the BG (green ROI in Fig. 6), whereas the right two boxes represent the results in the CSO (purple ROI in Fig. 6). In each region, both the cardiac and respiratory-related contributions are represented.

induced by respiratory cycle.

3.4. Volumetric strain

The volumetric strain is obtained by summing the observed strains over the three orthogonal directions. Fig. 7c shows the volumetric strains, which are largest in the deep brain (basal ganglia). Here, we observed cardiac-induced tissue expansion with median volumetric strain of $0.85 \cdot 10^{-3}$ (IQR: $0.39 \cdot 10^{-3}$ to $1.05 \cdot 10^{-3}$). For inspiration, a slight compression was observed with a median strain of $-0.28 \cdot 10^{-3}$ (IQR: $-0.41 \cdot 10^{-3}$ to $0.06 \cdot 10^{-3}$). A one-sided *t*-test revealed that both these observations were significantly different from zero ($p = 0.0008$ and $p = 0.047$, respectively). Although less pronounced, similar trends were observed in the CSO with cardiac-induced volumetric tissue expansion (median strain $0.28 \cdot 10^{-3}$ (IQR: 0 to $0.59 \cdot 10^{-3}$) and respiration-induced

volumetric tissue compression (median strain $-0.06 \cdot 10^{-3}$ (IQR: $-0.17 \cdot 10^{-3}$ to $0.20 \cdot 10^{-3}$)). Only the cardiac-induced volumetric tissue expansion was significantly different from zero in this region ($p = 0.02$ and $p = 0.7$, respectively).

4. Discussion

We developed a non-invasive method to measure brain tissue deformations resulting from cardiac and respiratory pulsations in the microvasculature that likely drive the brain's waste clearance system. The single-shot approach not only enabled us to unravel cardiac and respiratory contributions, but also allowed for an optimization of the tag spacing for strain measurements without introducing additional artifacts as are observed with multi-shot approaches (Soellinger et al., 2009; Adams et al., 2019). This optimization made analysis possible in small

ROIs, despite the amplified noise resulting from the use of spatial derivatives. For the CSO, we measured strain values comparable with values reported by Hirsch et al. (2013). We found larger strain values in the BG, which may reflect regional heterogeneity in tissue volumetric strain (and blood volume). We observed that the cardiac-induced strain in the microvasculature is larger than the respiration-induced strain, both for the volumetric strain as well as the 1D strain components in the three directions separately. B_0 offset fluctuations related to respiration decreased from the base of the brain to the top of the brain, and ranged typically between 0 and 10 Hz (Fig. 4), which compares well to the literature (Van Gelderen et al., 2007). This finding substantiates the credibility of the proposed model.

The observed systolic cardiac-induced tissue expansion is induced by the blood volume pulsations of the microvascular bed embedded in the tissue. Rivera et al. reported average relative volume pulsations of $0.3 \cdot 10^{-3}$ for gray matter and $0.1 \cdot 10^{-3}$ for white matter, respectively (Rivera-Rivera et al., 2019). These values are somewhat lower than our measurements, which is probably related to differences in methodology. We measured in small ROIs, while the 1D strain maps suggest considerable spatial variation in strain. Besides, we measured the tissue deformation directly, while Rivera et al. needed additional modeling to translate a measured T_2^* change induced by the injected contrast agent into a blood volume change via an estimated change in magnetic susceptibility. Mestre et al. reported a radius increase over the cardiac cycle of $\sim 1\%$ for arterioles (approximately $60\mu\text{m}$ in diameter) in mice (Mestre et al., 2018). The volumetric tissue strain ε associated with expansion of the microvascular bed is related to the relative cerebral blood volume (rCBV) by

$$\varepsilon = \frac{V_{\text{blood}}}{V_{\text{tissue}}} \delta \quad (11)$$

where $V_{\text{blood}}/V_{\text{tissue}}$ is the rCBV and δ is the relative change in blood volume. Assuming that the diameter change of 1% in arterioles is representative for the entire microvascular bed, and that the blood volume expansion is only due to the diameter increase of the blood vessels (i.e. elongation is negligible), the related relative blood volume change is $\sim 2\%$. Together with a rCBV of approximately 4% in gray matter and 2.5% in white matter (Bulte et al., 2007), the resulting volumetric tissue strains for gray and white matter are $0.8 \cdot 10^{-3}$ and $0.5 \cdot 10^{-3}$, respectively. Given the difference in species and the rather coarse estimation, these values estimated from observations in mice compare remarkably well with the volumetric strain we observed in humans, in the ROIs in BG (gray matter) and CSO (white matter), respectively.

In the interpretation of the observed volumetric strain values, it is important to note that these reflect in fact the net effect of both blood volume increase (microvascular expansion) and potential simultaneous compression of the interstitial space. The volumetric strain can be regarded as a lower bound estimation of the underlying blood volume pulsations, as any simultaneous compression of the interstitial space would reduce the amount of observable volumetric tissue strain. Comprehensive computer models that take the interaction between blood, CSF and tissue as porous medium (cells and interstitial fluid) into account could help to gain further insight into this effect (Linninger et al., 2005, 2009).

The respiratory effect found in this study implies loss of tissue volume due to venous outflow and is in accordance with the upward CSF flow through the spinal canal observed by Dreha-Kulaczewski et al. The observed tissue deformation due to respiration can only explain a small portion of the CSF flow found by Dreha-Kulaczewski (Dreha-Kulaczewski et al., 2017). However, in literature quite different results exist of the relative contributions of heartbeat and respiration cycles to CSF flow; some studies report dominant cardiac-related CSF flow (Daouk et al., 2017; Strik et al., 2002; Yildiz et al., 2017), while others identify respiration as the main driver of CSF flow (Dreha-Kulaczewski et al., 2015; Yamada et al., 2013), especially in the spinal canal (Dreha-Kulaczewski

et al., 2017). Moreover, one should note that the CSF flow does not only occur because of loss of tissue volume, but probably also due to compression of the larger veins that are embedded in the CSF (e.g. cortical veins and cavernous sinus) (Greitz et al., 1992). Venous compression seems to occur even during the cardiac cycle because the cortical veins behave as a Starling resistor, which facilitates back-propagation of the increased CSF pressure along the veins, thus preventing excessive pressure gradients across the capillary bed inside the brain tissue (DE Simone et al., 2017). Previous flow studies of respiration-related CSF flows, nor the current study assessed the volume of the larger veins. Future work should verify whether deflation of larger veins indeed dominate (upward) CSF flow during inspiration. Nevertheless, the current method helps to distinguish between the larger and smaller veins by providing a window to the microvasculature embedded in the tissue.

The proposed method allows for local assessment of tissue deformation and, thus, shows strong potential for studying mechanobiological processes of the brain. The results reveal interesting details of the deformation experienced by the brain's tissue including anisotropic strain that is consistent with the Poisson effect, which could be observed in a local ROI of only 3×3 pixels. Given that the brain is a porous medium (Goriely et al., 2015), we speculate that large tissue deformation could locally 'choke' the tissue by systolic compression of the (venous) microvasculature (Wirth et al., 2014). If such a choke-mechanism exists, it is conceivable that this may contribute to the appearance of white matter hyperintensities (WMH) as observed in patients with cerebral small vessel disease (Wardlaw et al., 2013a, 2013b). These WMH tend to form at the corners of the brain's ventricles, exactly at the location where we observe large tissue deformations in the coronal slice (see Fig. 6), and where intravascular pressures are relatively low, at the end of the vascular tree (Blanco et al., 2017). It is less speculative to state that the observed deformations play an important role in cellular gene expression and, thus, in maintaining brain tissue and vascular integrity (Dai et al., 2004; Goriely et al., 2015; Tarbell et al., 2014). Moreover, the brain tissue deformations are one of the drivers of the clearance system, as the deformation of the interstitial space contributes to the mixing and flow of the interstitial fluid and CSF (Tarasoff-Conway et al., 2015; Mestre et al., 2018; Asgari et al., 2016; Bakker et al., 2016). Brain clearance is currently mainly studied in animals. Mestre et al. found in mice that the relative contribution of the cardiac cycle to the flow velocity of the perivascular fluid was approximately a factor of five larger than the contribution of the respiration cycle (Mestre et al., 2018). We found a compatible difference in the contribution to the tissue volumetric strain between cardiac and respiratory cycles. Although further research is needed to justify direct comparison between tissue deformation and perivascular fluid flows, these results suggest that our method has potential to reduce the gap between invasive preclinical research and non-invasive observations in humans.

At the same time, it must be acknowledged that the driving forces of clearance are still under debate. The wavelength of the cardiac-related pulsations appears to be too long to induce significant spatial gradients that are needed for transport (Aldea et al., 2019). Vasomotion (spontaneous arterial diameter fluctuations initiated by vascular smooth muscle cells) occurs at a much lower frequency of approx. 0.1 Hz and with much shorter wavelengths. Indeed, recent animal work has shown that vasomotion is an important driver in clearance (van Veluw et al., 2019). Still, vascular pulsations may contribute to the clearance process through dispersion, which is a combined effect of mixing and diffusion (Asgari et al., 2016). It is unclear whether vasomotion is sufficiently spatially coherent to lead to measureable tissue strains, and whether our method would be sensitive enough to detect those low frequencies. The duration between motion encoding and decoding is limited by the T_1 tissue relaxation time, which is less than 2 seconds in the human brain at 7T. Still, we were also able to detect respiration-related effects, which have a frequency of approx. 0.25 Hz, not too far from the vasomotion frequency. Targeting potential vasomotion effects with our method would be an

interesting topic for future investigations.

The results showed different tissue deformation between gray matter (ROI in BG) and white matter (ROI in CSO) in healthy volunteers. The fact that the technique is sensitive enough to see normal regional differences in physiology in healthy people indicates that it also has potential for detecting abnormalities in tissue deformation in disease. As such, the technique may help in advancing our understanding of diseases like cerebral small vessel disease and the vascular contributions to neurodegenerative diseases. Currently, it is a limitation of this study that we could assess the tissue strain in a 2D slice and perform a volumetric strain analysis along a single line only. We therefore cannot infer respiration-related strains of the complete brain, as were recently performed for cardiac-induced strains (Adams et al., 2020). The sequence, however, holds the potential to extend the current 2D approach to a multi-slice acquisition, where the time between the cardiac phases is used to acquire additional slices at different locations in the brain. Such an approach would enable the acquisition of a 3D volume, without sacrificing any SNR and preserving the single-shot approach. It should also be investigated whether the proposed method – possibly extended to a multi-slice acquisition approach – can tolerate a 3/7 factor reduction in SNR, so that it can be implemented on 3T clinical scanners. A further limitation of this study is that no additional geometric EPI distortion corrections were performed, apart from 2nd order image based shimming. Although the analysis was performed in homogenous regions of the brain, geometric EPI distortion corrections would be necessary for regions with significant B_0 inhomogeneities (e.g. near the nasal cavities) through the use of an acquired B_0 -field map.

In conclusion, the developed single-shot 2D DENSE method is capable to consistently disentangle cardiac-related brain deformations from respiration-induced brain tissue deformations. We have successfully measured the separate contributions in small ROIs, despite the amplified noise induced by the use of spatial derivatives and found results that are consistent with physiological blood volume changes. This novel method provides a tool to directly study tissue dynamics that reflect fundamental aspects of the microvascular function and that holds potential to serve as a physiological marker of the waste clearance system of the brain.

Data availability

The data that support the findings of this study are available from the corresponding author upon request.

Code availability

The custom MATLAB software that was used for offline analysis of the data is available from the corresponding author upon request.

CRediT authorship contribution statement

Jacob Jan Sloots: Software, Visualization, Data curation, Formal analysis, Writing - original draft. **Geert Jan Biessels:** Supervision, Funding acquisition, Writing - review & editing. **Jaco J.M. Zwanenburg:** Supervision, Conceptualization, Methodology, Funding acquisition, Writing - review & editing.

Acknowledgments

The research leading to these results was supported by Vici Grant 918.16.616 from the Netherlands Organization for Scientific Research (NWO); the European Research Council under the European Union's Seventh Framework Programme (FP7/2007–2013)/ERC grant agreement no. 337333 and the European Union's Horizon 2020 research and innovation programme under grant agreement no. 666881.

Appendix A. Supplementary data

Supplementary data to this article can be found online at <https://doi.org/10.1016/j.neuroimage.2020.116581>.

References

- Adams, A.L., Kuijff, H.J., Viergever, M.A., Luijten, P.R., Zwanenburg, J.J.M., 2019. Quantifying cardiac-induced brain tissue expansion using DENSE. *NMR Biomed.* 32 e4050.
- Adams, A.L., Viergever, M.A., Luijten, P.R., Zwanenburg, J.J.M., 2020. Validating faster DENSE measurements of cardiac-induced brain tissue expansion as a potential tool for investigating cerebral microvascular pulsations. *Neuroimage* 208, 116466.
- Aldea, R., Weller, R.O., Wilcock, D.M., Carare, R.O., Richardson, G., 2019. Cerebrovascular smooth muscle cells as the drivers of intramural periarterial drainage of the brain. *Front. Aging Neurosci.* 11, 1.
- Aletas, A.H., Ding, S., Balaban, R.S., Wen, H., 1999. DENSE: displacement encoding with stimulated Echoes in cardiac functional MRI. *J. Magn. Reson.* 137, 247–252.
- Alperin, N.J., Lee, S.H., Loth, F., Raksin, P.B., Lichter, T., 2000. MR-intracranial pressure (ICP): a method to measure intracranial elastance and pressure noninvasively by means of MR imaging: baboon and human study. *Radiology* 217, 877–885.
- Asgari, M., de Zélécourt, D., Kurtcuoglu, V., 2016. Glymphatic solute transport does not require bulk flow. *Sci. Rep.* 6, 38635.
- Bakker, E.N.T.P., et al., 2016. Lymphatic clearance of the brain: perivascular, paravascular and significance for neurodegenerative diseases. *Cell. Mol. Neurobiol.* 36, 181–194.
- Bammer, R., 2003. Basic principles of diffusion-weighted imaging. *Eur. J. Radiol.* 45, 169–184.
- Bianciardi, M., et al., 2009. Sources of functional magnetic resonance imaging signal fluctuations in the human brain at rest: a 7 T study. *Magn. Reson. Imaging* 27, 1019–1029.
- Blanco, P.J., Müller, L.O., Spence, J.D., 2017. Blood pressure gradients in cerebral arteries: a clue to pathogenesis of cerebral small vessel disease. *Stroke Vasc. Neurol.* 2, 108–117.
- Bulte, D., Chiarelli, P., Wise, R., Jezard, P., 2007. Measurement of cerebral blood volume in humans using hyperoxic MRI contrast. *J. Magn. Reson. Imag.* 26, 894–899.
- Dai, G., et al., 2004. Distinct endothelial phenotypes evoked by arterial waveforms derived from atherosclerosis-prone and atherosclerosis-protected regions of the human vasculature. *Cardiovasc. Pathol.* 13, 26.
- Daouk, J., Bouzerar, R., Baledent, O., 2017. Heart rate and respiration influence on macroscopic blood and CSF flows. *Acta Radiol.* 58, 977–982.
- De Simone, R., Ranieri, A., Bonavita, V., 2017. Starling resistors, autoregulation of cerebral perfusion and the pathogenesis of idiopathic intracranial hypertension. *Panminerva Med.* 59, 76–89.
- Dreha-Kulaczewski, S., et al., 2015. Inspiration is the major regulator of human CSF flow. *J. Neurosci.* 35, 2485–2491.
- Dreha-Kulaczewski, S., et al., 2017. Identification of the upward movement of human CSF in vivo and its relation to the brain venous system. *J. Neurosci.* 37, 2395–2402.
- Feinberg, D.A., Mark, A.S., 1987. Human brain motion and cerebrospinal fluid circulation demonstrated with MR velocity imaging. *Radiology* 163, 793–799.
- Fischer, S.E., McKinnon, G.C., Maier, S.E., Boesiger, P., 1993. Improved myocardial tagging contrast. *Magn. Reson. Med.* 30, 191–200.
- Goriely, A., et al., 2015. Mechanics of the brain: perspectives, challenges, and opportunities. *Biomech. Model. Mechanobiol.* 14, 931–965.
- Greitz, D., et al., 1992. Pulsatile brain movement and associated hydrodynamics studied by magnetic resonance phase imaging. The Monroe-Kellie doctrine revisited. *Neuroradiology* 34, 370–380.
- Helenius, J., et al., 2002. Diffusion-weighted MR imaging in normal human brains in various age groups. *AJNR Am J Neuroradiol* 23, 194–199.
- Hirsch, S., et al., 2013. In vivo measurement of volumetric strain in the human brain induced by arterial pulsation and harmonic waves. *Magn. Reson. Med.* 70, 671–682.
- Kiviniemi, V., et al., 2016. Ultra-fast magnetic resonance encephalography of physiological brain activity – glymphatic pulsation mechanisms? *J. Cerebr. Blood Flow Metabol.* 36, 1033–1045.
- Klein, S., Staring, M., Murphy, K., Viergever, M.A., Pluim, J.P.W., 2010. Elastix: a toolbox for intensity-based medical image registration. *IEEE Trans. Med. Imag.* <https://doi.org/10.1109/TMI.2009.2035616>.
- Linninger, A.A., et al., 2005. Pulsatile cerebrospinal fluid dynamics in the human brain. *IEEE Trans. Biomed. Eng.* 52, 557–565.
- Linninger, A.A., et al., 2009. A mathematical model of blood, cerebrospinal fluid and brain dynamics. *J. Math. Biol.* 59, 729–759.
- Linninger, A.A., Tangen, K., Hsu, C.-Y., Frim, D., 2016. Cerebrospinal fluid mechanics and its coupling to cerebrovascular dynamics. *Annu. Rev. Fluid Mech.* 48, 219–257.
- Mestre, H., Kostrikov, S., Mehta, R.L., Nedergaard, M., 2017. Perivascular spaces, glymphatic dysfunction, and small vessel disease. *Clin. Sci.* 131, 2257–2274.
- Mestre, H., et al., 2018. Flow of cerebrospinal fluid is driven by arterial pulsations and is reduced in hypertension. *Nat. Commun.* 9, 4878.
- Mokri, B., 2001. The Monroe-Kellie hypothesis: applications in CSF volume depletion. *Neurology* 56, 1746–1748.
- Pahlavan, S.H., Oshinski, J., Zhong, X., Loth, F., Amini, R., 2018. Regional quantification of brain tissue strain using displacement-encoding with stimulated Echoes magnetic resonance imaging. *J. Biomech. Eng.* 140, 081010.

- Polimeni, J.R., et al., 2016. The pulsatility volume index: an indicator of cerebrovascular compliance based on fast magnetic resonance imaging of cardiac and respiratory pulsatility. *Philos. Trans. R. Soc. A Math. Phys. Eng. Sci.* 374, 20150184.
- Reese, T.G., Feinberg, D.A., Dou, J., Wedeen, V.J., 2002. Phase contrast MRI of myocardial 3D strain by encoding contiguous slices in a single shot. *Magn. Reson. Med.* 47, 665–676.
- Rivera-Rivera, L.A., Johnson, K.M., Turski, P.A., Wieben, O., Schubert, T., 2019. Measurement of microvascular cerebral blood volume changes over the cardiac cycle with ferumoxytol-enhanced T2* MRI. *Magn. Reson. Med.* <https://doi.org/10.1002/mrm.27670>.
- Rooney, W.D., et al., 2007. Magnetic field and tissue dependencies of human brain longitudinal 1H2O relaxation in vivo. *Magn. Reson. Med.* 57, 308–318.
- Sack, I., Streiberger, K.J., Krefting, D., Paul, F., Braun, J., 2011. The influence of physiological aging and atrophy on brain viscoelastic properties in humans. *PLoS One* 6.
- Sloots, J.J., Luijten, P.R., Biessels, G.J., Zwanenburg, J.J.M., 2019a. Cardiac and respiratory induced 3D brain tissue strain as marker of physiological blood volume dynamics at 7T MRI. *ISMRM Proc* 2799.
- Sloots, J.J., Luijten, P.R., Biessels, G.J., Zwanenburg, J.J.M., 2019b. Optimizing the DENSE sequence for accurate brain tissue strain measurements at 7T MRI. *ISMRM Proc* 2800.
- Soellinger, M., Rutz, A.K., Kozerke, S., Boesiger, P., 2009. 3D cine displacement-encoded MRI of pulsatile brain motion. *Magn. Reson. Med.* 61, 153–162.
- Spector, R., Robert Snodgrass, S., Johanson, C.E., 2015. A balanced view of the cerebrospinal fluid composition and functions: focus on adult humans. *Exp. Neurol.* 273, 57–68.
- Ståhlberg, F., et al., 1989. A method for MR quantification of flow velocities in blood and CSF using interleaved gradient-echo pulse sequences. *Magn. Reson. Imaging* 7, 655–667.
- Strik, C., Klose, U., Erb, M., Strik, H., Grodd, W., 2002. Intracranial oscillations of cerebrospinal fluid and blood flows: analysis with magnetic resonance imaging. *J. Magn. Reson. Imag.* 15, 251–258.
- Tarasoff-Conway, J.M., et al., 2015. Clearance systems in the brain - implications for Alzheimer disease. *Nat. Rev. Neurol.* 11, 457–470.
- Tarbell, J.M., Simon, S.I., Curry, F.-R.E., 2014. Mechanosensing at the vascular interface. *Annu. Rev. Biomed. Eng.* 16, 505–532.
- Tsao, C.W., et al., 2013. Relations of arterial stiffness and endothelial function to brain aging in the community. *Neurology*. <https://doi.org/10.1212/WNL.0b013e3182a43e1c>.
- Van Gelderen, P., De Zwart, J.A., Starewicz, P., Hinks, R.S., Duyn, J.H., 2007. Real-time shimming to compensate for respiration-induced B0 fluctuations. *Magn. Reson. Med.* 57, 362–368.
- van Veluw, S.J., et al., 2019. Vasomotion as a driving force for paravascular clearance in the awake mouse brain. *Neuron*. <https://doi.org/10.1016/J.NEURON.2019.10.033>.
- Viessmann, O., Möller, H.E., Jezzard, P., 2017. Cardiac cycle-induced EPI time series fluctuations in the brain: their temporal shifts, inflow effects and T2* fluctuations. *Neuroimage* 162, 93–105.
- Wardlaw, J.M., Smith, C., Dichgans, M., 2013a. Mechanisms of sporadic cerebral small vessel disease: insights from neuroimaging. *Lancet Neurol.* 12, 483–497.
- Wardlaw, J.M., et al., 2013b. Neuroimaging standards for research into small vessel disease and its contribution to ageing and neurodegeneration. *Lancet Neurol.* 12, 822–838.
- Wirth, B., Sobey, I., Eisentrager, A., 2014. Conditions for choking in a poroelastic flow model. *IMA J. Appl. Math.* 79, 254–273.
- Yamada, S., et al., 2013. Influence of respiration on cerebrospinal fluid movement using magnetic resonance spin labeling. *Fluids Barriers CNS* 10, 36.
- Yildiz, S., et al., 2017. Quantifying the influence of respiration and cardiac pulsations on cerebrospinal fluid dynamics using real-time phase-contrast MRI. *J. Magn. Reson. Imag.* 46, 431–439.